FINITE ELEMENT MODELING OF HOLLOW PRECAST PRESTRESSED REINFORCED CONCRETE PILES

Steven M. Greenwood, Dept. of Civil Engineering, Washington State University
William F. Cofer, PhD, PE, Dept. of Civil Engineering, Washington State University
Mohamed A. ElGawady, PhD, Dept. of Civil Engineering, Washington State University
David I. McLean, PhD, PE, Dept. of Civil Engineering, Washington State University

Previous research has shown that circular hollow precast prestressed reinforced concrete piles have limited ductile response under cyclic loading. In order to understand the response and failure mechanisms for piles of this configuration, nonlinear finite element analyses were performed. Analytical models for predicting the performance of these piles under bending and axial loads have been developed using two methods; ABAQUS/Standard, and XTRACT in conjunction with SAP2000. Both models were verified against existing experimental data.

This paper presents the results of both the detailed (ABAQUS) and simplified (XTRACT/SAP2000) analyses and the material model definitions required for them. Both models simulate the response of the tested piles reasonably well. However, careful consideration must be taken when implementing concrete model options in ABAQUS such as compression hardening, tension stiffening and damage. In addition, the plastic hinge length specified in the SAP2000 analyses governs performance. Consequently, a method for determining material characteristics such as compressive strength, tensile strength, fracture energy, crack mouth opening width, and compressive/tensile damage has been developed. The method utilized is based primarily on fundamental fracture mechanics and reinforced concrete design.

Keywords: finite element; FEA; prestressed; precast; reinforced concrete; piles; nonlinear; inelastic; hollow; foundations.

INTRODUCTION

Pile foundations are used throughout the world in a wide variety of soil types and applications. Commonly, piles are used in the construction of single/multiple column bent bridge foundations. Recent research pertaining to the cyclic performance of circular hollow precast prestressed reinforced concrete piles has shown that numerous deficiencies exist.[1,2] In order to understand the behavior and failure mechanisms of hollow precast prestressed reinforced concrete piles, a series of inelastic nonlinear analyses have been performed. Once failure mechanisms are qualitatively and quantitatively understood, efforts can be focused on developing viable retrofit methods for pile foundations of this type.

The objective of this work is to present two different analytical models for analysis of circular hollow prestressed concrete piles under lateral load. The first is a detailed finite element model using ABAQUS/Standard[3]. The second is a simplified analytical model using XTRACT[4] in conjunction with SAP2000[5]. The models were verified against existing experimental data in order to confirm performance with respect to failure mechanisms and load and ductility capacity.

BACKGROUND

In 1997, Budek, et al.[1] performed a series of nonlinear inelastic analyses of hollow prestressed pile foundations modeled as Winkler beams. Pile behavior was based on moment-curvature analysis up to the ultimate concrete compression strain. The prestressed piles exhibited limited ductility that was severely degraded at high levels of axial load.

To further investigate analysis results, Budek, Benzoni and Priestley[2] tested four circular hollow prestressed pile configurations under cyclic loading. The authors investigated the effects of varying the volumetric transverse reinforcement ratio, inclusion/exclusion of non-prestressed longitudinal reinforcement through the expected plastic hinge region and varying external confinement. External confinement was supplied by rubber pads, which lined the saddles used to apply loading. The hollow piles tested exhibited minimal energy-absorbing hysteretic behavior and displayed essentially nonlinear-elastic response. Varying levels of transverse reinforcing steel and external confinement had minimal influence on displacement capacity. Failure was violent and abrupt, occurring when the core strain reached a value of approximately 0.004. The failure mechanism generally observed in the tests was spalling followed by loss of the compression zone.

PILE GEOMETRY AND LOADING

The finite element model proposed in this document was generated in an attempt to reproduce the response of the specimens denoted by Budek, et al.[2] as PS12 and PS13. A brief summary of the pile specifications and loading devices follows.

An overview of the testing apparatus is provided in Figure 1. The test fixture was assembled such that the pile could be considered as a simply supported flexure member. The concrete compressive strength for both piles was approximately 67 MPa (9700 psi). The piles measured 7315 mm (288 in.) in overall length, 6100 mm (240 in.) between supports. The pile was constructed with a 610 mm (24 in.) outer diameter and 422 mm (16.6 in.) inner diameter, resulting in a wall thickness of 94 mm (3.7 in.).

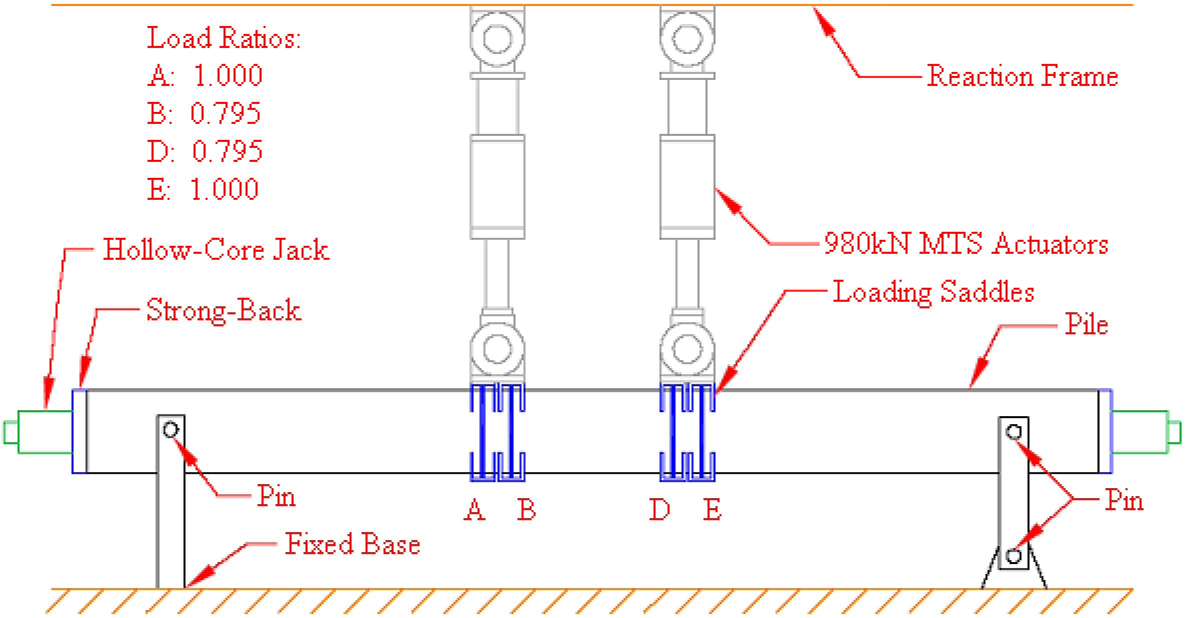

Fig. 1: Arrangement of Test Apparatus[2]

Transverse shear reinforcement was supplied by a 515.7 mm (20.3 in.) diameter W8 A82 wire spiral pitched at 76 mm (3 in.), resulting in 41 mm (1.6 in.) of concrete cover and a nominal transverse reinforcement ratio of 0.2 percent. The yield and ultimate strength of the transverse reinforcing steel were reported as 647 MPa (94 ksi) and 816 MPa (118 ksi), respectively. Prestressing steel consisted of sixteen 12.7 mm (0.5 in.) 7-wire strands stressed at 744 MPa (108 ksi) after losses. The yield and ultimate strength of the prestressing strands were reported as 1585 MPa (230 ksi) and 1860 MPa (270 ksi), respectively. The sole difference between the two specimens was the inclusion of longitudinal reinforcement through the plastic hinge region of PS13 using eight M#13 455 MPa (#4 Gr. 60 ksi) nominal yield strength rebars.

A whiffle tree loading apparatus with two actuators was used to simulate the moment pattern expected from lateral earth pressure on the pile. Loading saddles were lined with rubber pads, which were selected to simulate the soil subgrade reaction modulus. An externally applied axial load was supplied to produce a nominal value of $0.12f_c'A_g$, where f_c' is the concrete compressive strength and A_g is the gross area of the cross section.

XTRACT MODELING

Prior to ABAQUS/Standard modeling, the PS12 and PS13 specimens were modeled using the XTRACT software[4]. XTRACT utilizes two dimensional discretization to determine moment, curvature, stress, and strain in a user defined cross section. The pile cross section was modeled to the specifications detailed in the background section of this document. Prestressing steel was defined using the high strength prestressing steel model with nominal properties pertaining to A416 Gr. 270 ksi steel. Longitudinal rebar was defined using a bilinear steel model with strain hardening and nominal properties of A615 Gr. 60 ksi steel. Nominal properties of the steel models used are predefined options available in XTRACT.

In order to fully define the concrete in the model, the tensile strength, elastic modulus, yield stress, crushing, spalling, and failure strains must be supplied. Stress and strain values at yield, maximum compressive stress, and ultimate compressive stress were obtained from standard references[6]. The elastic modulus was defined using Equation 1, a metric conversion of the equation per ACI318-05[7].

$$E_c = 4733\sqrt{f_c^{'}} \tag{1}$$

Where:

f_c' = *Unconfined concrete compressive strength (MPa)*

The tensile strength, taken as the cylinder splitting strength defined by Iravani[8], is presented in Equation 2, with f_c' as previously defined.

$$f_{sp}^{'} = 0.57\sqrt{f_c^{'}} \tag{2}$$

Based on the report by Budek, et al.[2], it was observed that sudden catastrophic failure of the pile specimen occurred shortly after cover concrete began to spall. Therefore, the spalling strain is an important indicator of failure and both it and crushing strain were taken as ε_{cu} = 0.0027 from recommendations by Bae and Bayrak[9]. The strain at which the analysis was terminated, the failure strain, was thus defined as 0.003.

Moment-curvature analysis was carried out until the failure strain of 0.003 was achieved. Loading for the cross sectional analysis was applied in the form of an 890 kN (200 kip) ‘first step’ axial load with an incrementing moment about the x-axis. Discussion and results from the 2D cross section analyses can be found in the results section of this study.

ABAQUS MODELING

In order to qualitatively understand failure mechanisms and quantify the onset of failure, static analyses of three dimensional pile models were performed using ABAQUS/Standard version 6.7[3]. ABAQUS/CAE version 6.7 was predominantly used to generate the 3D pile models. Constitutive theories used in development of the finite element models are available in the ABAQUS/Standard material library and are described in the ABAQUS user's manual.[3]

CONSTITUTIVE MODELS

Concrete

The pile concrete utilized the density, elastic, and concrete damaged plasticity models defined in the ABAQUS material library. Unit weight of the concrete was taken as 22.8 kN/m^3 (145 lb$_f$/ft^3). The elastic properties were defined by a Poisson's ratio of 0.15 and Young's modulus of 38741 MPa (5619 ksi) from Equation 1. The concrete damaged plasticity option was used to define the yield surface, viscosity parameters, and flow potential in the damaged plasticity model. In addition, the concrete compression and concrete tension damage options were also incorporated in the constitutive model to simulate damage of the concrete due to tensile cracking and compressive crushing.

Five parameters are required to fully describe the damaged plasticity option: the dilation angle in degrees, the flow potential eccentricity, the ratio of initial equibiaxial compressive yield stress to initial uniaxial compressive yield stress, the ratio of the second stress invariant on the tensile meridian to that on the compressive meridian, and the viscosity parameter that defines visco-plastic regularization.[3] The aforementioned parameters were set to 15°, 0.1, 1.16, 0.66, and 0.01, respectively, as recommended.[3]

Compression behavior of the concrete was defined by compressive stress and corresponding inelastic strain data. Stress-strain data was obtained by selecting four points from a typical stress strain curve.[6] The four points selected correspond to yield, maximum compressive stress, ultimate compressive stress, and ~7 percent of maximum compressive stress, which defined the concrete behavior after crushing. A complete loss of strength in compression was not considered, primarily to avoid any potential convergence issues that would arise once compressive stress reached zero in a given element. Strain values obtained from the stress-strain curve were then defined in terms of plastic strain by subtracting the strain at yield from the values of total strain. An example of the idealized stress-strain definition is provided in Figure 2.

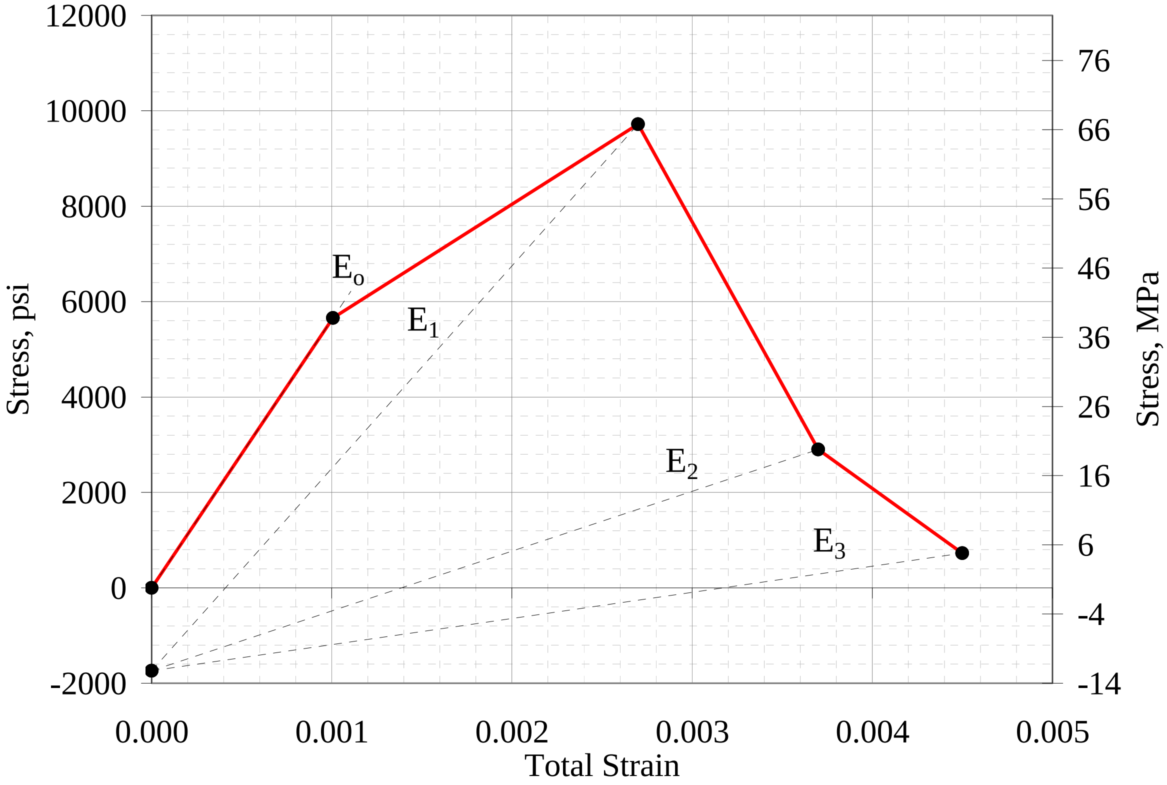

Fig. 2: Idealized Compressive Stress-Strain Relationship

Tensile behavior of the concrete was defined using a fracture energy cracking criterion since significant regions of the models do not contain reinforcing steel. In this case, the brittle behavior of concrete is described using a stress-displacement relationship based on Hillerborg's[10] fracture energy proposal, which defines fracture energy, G_f, as the energy required to open a crack of unit area. The fracture energy cracking model available in ABAQUS can be invoked in two ways: specifying fracture energy as a material property in which tensile stress is a linear tabular function of fracture energy, or specifying postfailure stress as a tabular function of crack displacement.[3] The former definition was used in development of the PS12 and PS13 FEA models. The use of the selected definition for tensile behavior requires the following three parameters: fracture energy, tensile stress associated with initiation of cracking (f_{sp}), and the crack opening displacement at which a complete loss of strength is specified to occur (u_0). A schematic of the stress-displacement relationship is presented in Figure 3.

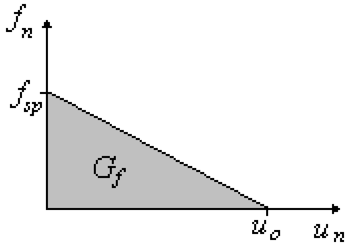

Fig. 3: Tensile Stress-Displacement Behavior

To determine the fracture energy associated with the 67 MPa (9700 psi) concrete, a fracture mechanics approach was used. From fracture mechanics in plane stress applications[11], fracture energy is defined in Equation 3 as:

$$G_f = \frac{K_{if}^2}{E} \tag{3}$$

Where:

G_f = Fracture energy required to initiate tensile cracking (Force/Length)
K_{if} = Stress intensity factor for a plate of infinite size (Force/Length$^{3/2}$)
$E = E_c$ = Elastic modulus for concrete (Force/Length^2)

The stress intensity factor for a plate of infinite size[12] is defined by Equation 4:

$$K_{if} = 1.12\sigma\sqrt{\pi a} \tag{4}$$

Where:

$\sigma = f_{sp}$ = Concrete cylinder splitting strength (Force/Length^2)
a = Crack depth (Length)

Equations 3 and 4 are applicable for any consistent set of units. The elastic modulus of concrete and tensile splitting strength were calculated using Equations 1 and 2, respectively. The crack depth used to define the stress intensity factor was taken as 43 mm (1.69 in.) which corresponds to the depth of concrete cover to transverse reinforcing steel. The resulting calculated value of fracture energy was 0.095 N/mm (0.542 lb_f/in.). It was found that the calculated value for G_f agreed with results presented by Roesler, et al.[11], Darwin, et al.[13], Appa Rao and Raghu Prasad[14], and Einsfeld and Velasco[15] for concrete mixes of similar design strength. Using the calculated values for fracture energy and concrete cylinder splitting strength, the crack displacement associated with complete loss of tensile capacity, u_o, was calculated from Equation 5. The resulting crack displacement was calculated as 0.041 mm (1.61 x 10^{-3} in.).

$$u_o = \frac{2G_f}{f_{sp}} \tag{5}$$

Compression damage of the concrete is prescribed by tabular data which specifies the decimal percentage of stiffness degradation at corresponding values of plastic strain. Values of stiffness degradation, d_c, were calculated via Equation 6. A graphic representation of stiffness degradation can be viewed in Figure 2, represented by moduli E_1, E_2, and E_3.

$$d_c = 1 - \frac{E_n}{E_o} \tag{6}$$

Where:

$E_n = E_1, E_2, E_3$ = Values of degraded elastic modulus
E_o = Initial elastic modulus

Values for the degraded elastic modulus were calculated as the slope of the line connecting points (0 , σ_{ret}) and ($\varepsilon_{c,i}$, $\sigma_{c,i}$) where σ_{ret} is the value of tensile stress to ensure that negative plastic strain values will not evolve and ($\varepsilon_{c,i}$, $\sigma_{c,i}$) are the total strain and stress values for a given point on the idealized stress-strain curve. It was determined for this work that σ_{ret} should be taken as approximately 18 percent of the concrete compressive strength and an additional five percent reduction in the compression damage values was necessary in order to avoid numerical convergence issues. The resulting value for stiffness degradation for plastic strains of 0, 0.0017, 0.0027, and 0.0035 were 0, 19, 73, and 85 percent, respectively. It was assumed that under cyclic loading, recovery of tensile stiffness after crack formation would not occur, therefore, the scalar multiple for tension recovery was nil.

Since the fracture energy type of tension stiffening was employed, tension damage criteria were prescribed as a tabular function of crack displacement, u_n. It was assumed that, at a complete loss of tensile strength ($u_n = u_o$), stiffness of cracked elements would undergo a 50 percent degradation. In addition, once u_n was equivalent to $2u_o$, it was assumed that cracked elements would experience a 98 percent degradation in stiffness. One hundred percent degradation in stiffness was not utilized since values greater than 99 percent can drastically affect convergence[3]. It was assumed that full recovery of compression stiffness would occur in the event of cyclic loading; that is, tensile cracking has no effect on recovery of compression stiffness. As a result, the scalar multiple of compression recovery was assumed to be unity.

Elastic Concrete

To avoid unnecessary material nonlinearity at points of support, the material at the ends of the specimen were modeled as linearly elastic.

Hoop and Longitudinal Reinforcement

An elasto-plastic constitutive model was used to define the behavior of the hoop reinforcement and longitudinal steel. Unit weight of the steel was set as 77.0 kN/m^3 (490 lb_f/ft^3). An elastic modulus of 209 x 10^3 MPa (30.3 x 10^3 ksi) and a Poisson's ratio of 0.3 defined the elastic response. Plastic behavior was defined in terms of tabular stress-strain data.[6]

Prestressing Strands

The material used to define the prestressing tendon behavior incorporated the same options mentioned in the hoop and longitudinal reinforcement discussion. The material density prescribed was that stated for the longitudinal and hoop reinforcement. A Poisson's ratio of 0.3 was implemented, with an elastic modulus of 189.6 x 10^3 MPa (27.5 x 10^3 ksi). Plastic behavior of the prestressing steel was defined in terms of tabular stress-strain data.[6]

Rubber Pads

The constitutive model for the rubber pads was defined using only the elastic option since their contribution to gravity loads was both negligible and undesired. Since the manufacturer and rubber grade used in Reference 2 was undisclosed, a rubber material with a nominal durometer hardness of 70 was selected. Geolast® 701-70 Thermoplastic Rubber was the rubber selected for the FEA models. Material data was retrieved from MatWeb[16]. The elastic modulus was reported as 5.9 MPa (856 psi) with a Poisson's ratio of 0.5.

Saddle Steel

For modeling purposes, the loading saddles were assumed to be nearly rigid, with linear elastic properties.

MODEL GEOMETRY

Finite elements for the pile consisted of standard eight-node linear hexahedral 3D continuum elements with full integration. In order to simplify the modeling process, the rubber pads and loading saddles were modeled as part of the pile geometry. This eliminated the need for surface contact definitions between the rubber pads and the pile and loading saddles. It was expected that this simplification would be reasonable since the stiffness of the rubber pads was much less than the concrete and saddle stiffnesses.

The pile was meshed such that the approximate global size of each element was 30 mm (1.18 in.). In addition, 90 mm (3.54 in.) of each end of the pile were partitioned as cells to facilitate the use of the boundary conditions, which will be discussed later and will be referred to as the 'elastic ends'.

Spiral reinforcement was simplified into hoop reinforcement consisting of 80 discrete hoops with 76 mm (3 in.) spacing between each one. The end most hoops were placed 48 mm (1.89 in.) from the pile ends to facilitate symmetric spacing. Elements comprising the hoops were standard two-node 3D truss elements. The reinforcing hoop section had a cross sectional area of 51.5 mm^2 (0.08 $in.^2$) and the hoop reinforcement material definition.

Discrete prestressing tendons and longitudinal reinforcing bars were also composed of standard two-node 3D truss elements. The tendons measured 6100 mm (240 in.) in length, while longitudinal reinforcing bars measured 536.8 mm (21 in.) in length based on the estimated length of plastic hinge formation as presented in Reference 2. Meshes for the tendons and longitudinal rebar were automatically generated. The tendon section was assigned a cross-sectional area of 74 mm^2 (0.115 in.^{2}) and the prestressing steel constitutive model. Similarly, the rebar section was characterized using the hoop reinforcement material model and a 129 mm^2 (0.2 in.^{2}) area of cross section. The use of the hoop reinforcement constitutive model for the longitudinal rebar was deemed appropriate due to the variability in standard grades of reinforcing steel.

Prestressing tendons, transverse reinforcement, and longitudinal rebar (in the case of pile PS13) were included in the model assembly as embedded elements. Representations of the reinforcement layout and pile model assembly are presented in Figures 4 and 5, respectively.

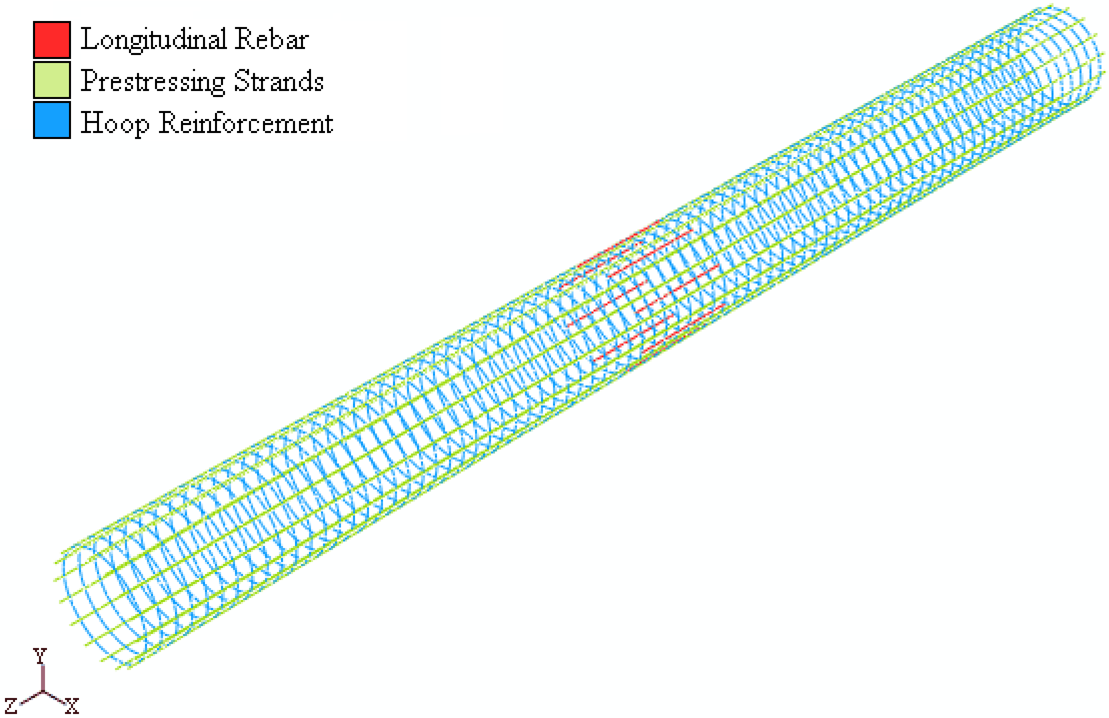

Fig. 4: ABAQUS Model Reinforcement Layout

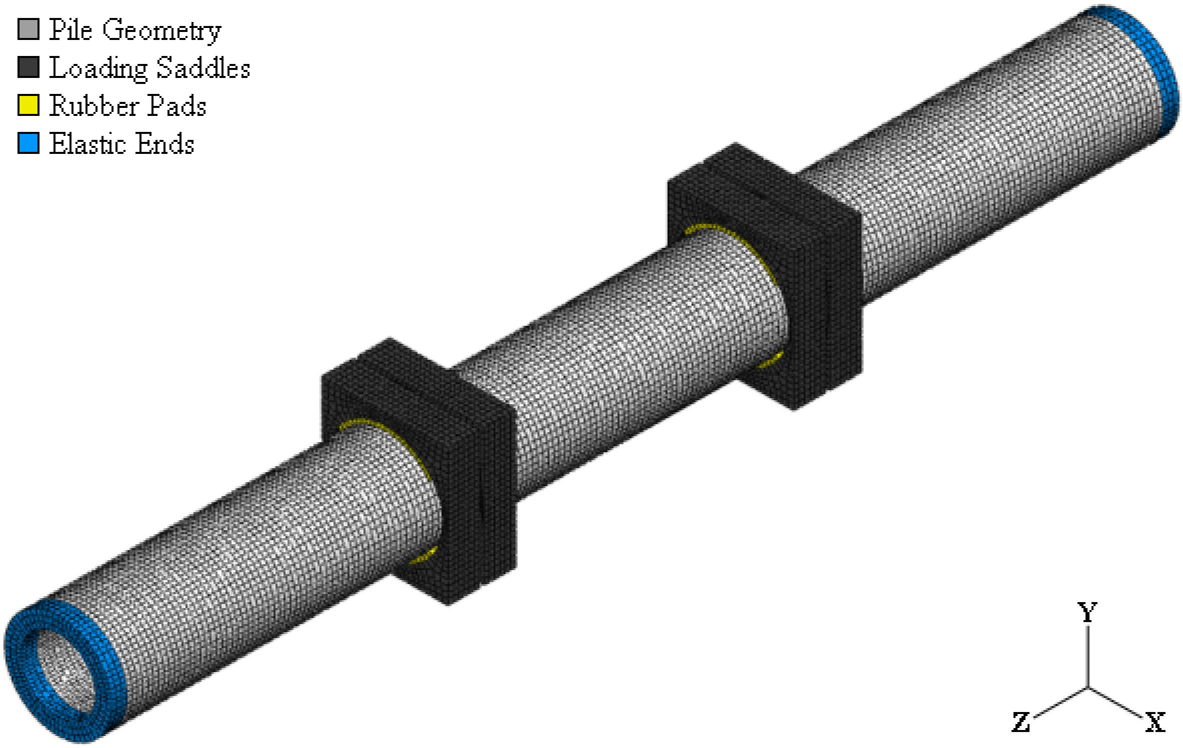

Fig. 5: Pile Model Assembly

BOUNDARY & INITIAL CONDITIONS

Please refer to Figure 5 throughout the description of the boundary conditions and loading. To simulate the support conditions as described in Reference 2, the *Ux*, *Uy* and *Uz* degrees of freedom (DOF) were constrained for selected centroidal nodes at the left end of the pile to simulate a pin support, while DOF *Ux* and *Uy* at the right end were similarly constrained to simulate the roller support. In order to avoid erroneous results and stress concentrations at the constrained boundary condition nodes, 90 mm (3.54 in.) at each end of the pile were defined by the aforementioned elastic concrete constitutive model. To facilitate generation of load-displacement plots, mid-span displacement in the *y*-direction was monitored during each increment of each loading step.

Prestressing was applied using a stress-type initial condition. Prestressing was supplied to the sixteen tendons at a magnitude of 744 MPa (107.9 ksi) in the *z*-direction. Although it was not expected to be significant, nonlinear geometry was considered during application of initial conditions. Gravity loads were also applied as an initial condition in the negative *y*-direction.

LOADING

Two loading steps were used for the analysis of the 3D pile model. For the first step, an axial load of 890 kN (200 kip) was applied at the roller supported end of the pile as a 5.84 MPa (847 psi) uniformly distributed pressure on the pile cross section in the positive *z*-direction.

This loading was prescribed as a non-following surface traction in order to account for moment evolution due to *P-Δ* effects. Nonlinear geometry due to large deformations and deflections was also included in the step definition.

The second loading step consisted of a monotonic push in the negative *y*-direction. The monotonic push was symmetric in nature about the *x-y* plane of symmetry at mid-span. Loading was defined as uniformly distributed ramped pressures applied to the top of each saddle. The maximum magnitude supplied to each of the two outer saddles was prescribed as 1.656 MPa (240 psi) and 79.5 percent of that for the interior two saddles. Nonlinear geometry due to extreme deformations and displacements was also considered during the monotonic push step of the analysis.

SAP2000 MODELING

In order to determine the force-displacement response of both piles, which is crucial for displacement based design, the moment curvature relationships developed in XTRACT were implemented in a simple pile model in SAP2000. A detailed discussion of the SAP2000 modeling procedure is described elsewhere.[17] Both piles were modeled as four-point bending, simply supported beams with a point plastic hinge defined at mid-span. The yield surface was defined by an axial load-effective yield moment interaction diagram. Post yielding behavior was defined by moment-curvature results from XTRACT for axial loads of 204, 890, and 1634 kN (46, 200, and 367 kips, respectively). The plastic hinge length (L_p) was defined according to Caltrans recommendations[18] for non-cased Type I pile shafts. The calculated plastic hinge length for both specimens was computed to be 1.40D, which was in close agreement with the observed plastic hinge lengths during the experimental work[2]. In order to illustrate the sensitivity of the SAP2000 results with respect to plastic hinge length, additional analyses were performed with L_p = 2.80D, twice that of the recommended value.

RESULTS

XTRACT ANALYSES

The section behavior at failure for the XTRACT model of PS12 is shown in Figure 6. Note that the overall performance of the model was governed by the tensile behavior of the concrete. Once tensile cracks form through the wall thickness, the size of the compression zone rapidly decreases as moment about the *x*-axis is increased. Results from the analysis show that once the compressive region was reduced to the extent that the compressive peak fiber strain is equivalent to the spalling strain, failure occurs. Moreover, the analysis becomes unstable and is terminated once concrete spalls to a depth roughly equivalent to the depth of cover, as illustrated in Figure 6.

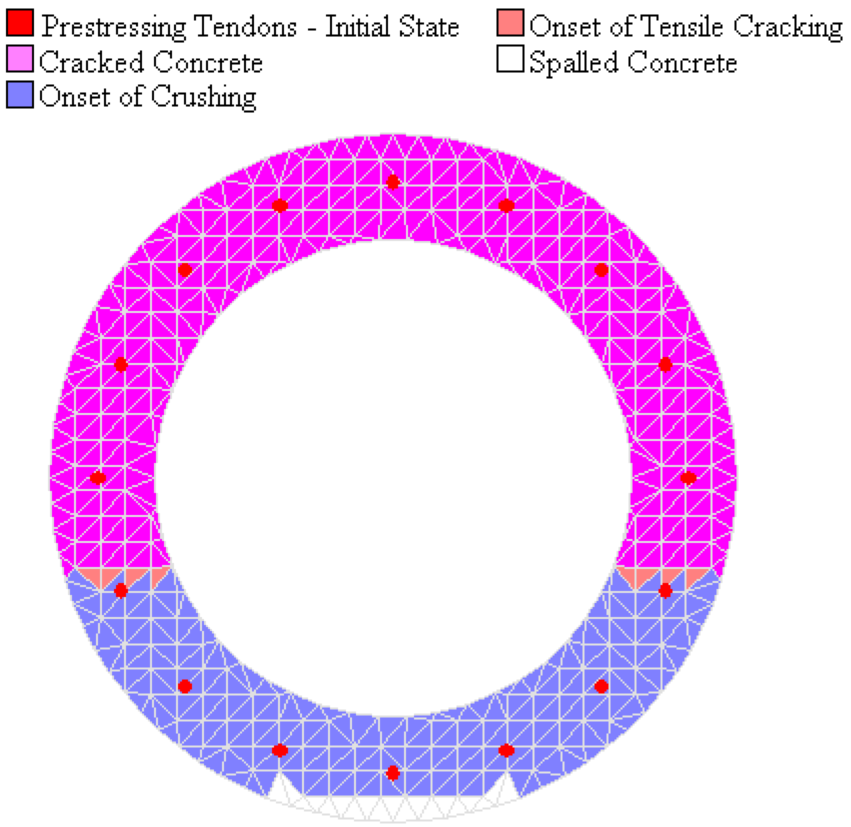

Fig. 6: PS12 Deformed Shape from XTRACT

The moment-curvature ductility response is given in Figure 7, compared with results transcribed from hysteretic curves reported by Budek, et al[2]. It should be noted that, in the experimental work, the yield curvature for PS12 and PS13 was defined as 0.0065 m^{-1} (0.0019 ft^{-1}) and 0.007 m^{-1} (0.0021 ft^{-1}), respectively. Curvature ductility is defined as the ratio of the curvature of the cross-section at any time, *t*, to curvature at yielding. Upon examination of the plot, one will see that XTRACT is able to accurately capture the elastic response of the PS12 pile model. Once curvature ductility of approximately 0.3 is reached, the results from the predictive model begin to diverge from those of Budek, et al.[2] It is important to note that the moment predicted for failure was within eight percent of that observed in the test. The model predicted only about half of the ultimate curvature ductility of the test, but damage from the cyclic loading of the test may have led to reduced stiffness after initial cracking that was not considered in the model.

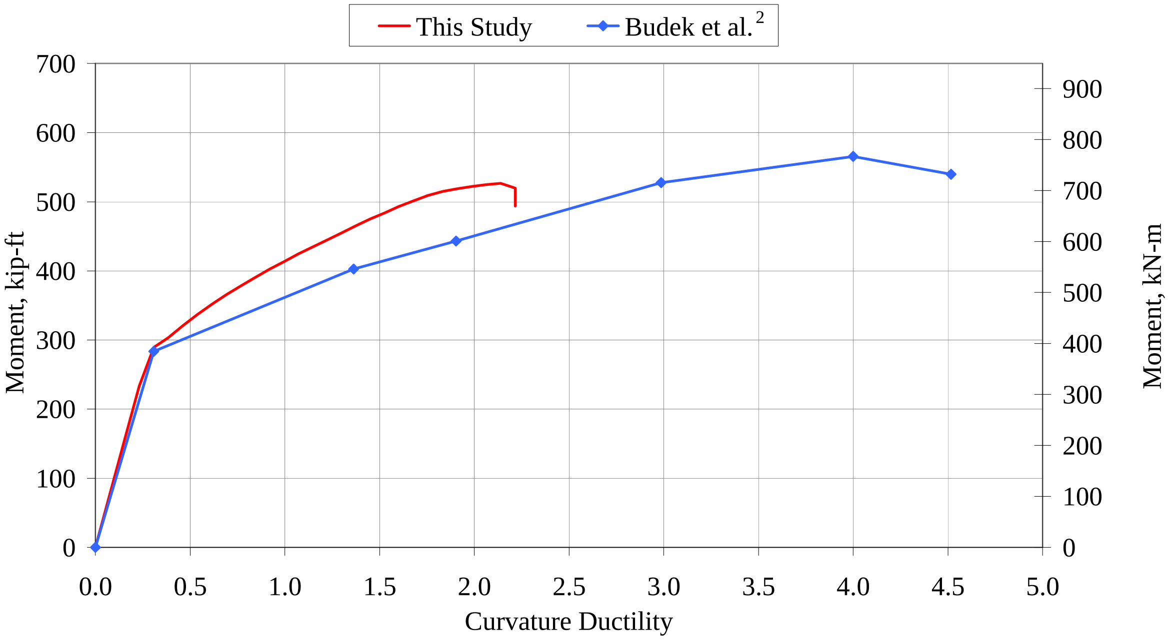

Fig. 7: Comparison of XTRACT and Test Results for PS12

The section behavior at failure of the XTRACT model for PS13 was nearly identical to that of PS12. Not unlike the XTRACT model for PS12, performance was governed by the tensile capacity of the concrete. Failure of specimen PS13 occurred when the peak fiber strain was equivalent to the spalling strain. At that juncture, the depth of spalling was roughly equivalent to the depth of concrete cover. In addition, the model became unstable and the analysis was terminated. The moment-curvature ductility response of PS13 is provided in Figure 8, again compared to the results of from Reference 2. Much closer agreement was obtained, possibly due to reduced concrete damage during cyclic loading with the added reinforcement. Examination of the plot illustrates the fact that the model is able to reasonably capture the elastic and inelastic response of the pile. Analytical results for the moment capacity and curvature ductility is accurately predicted up to a curvature ductility of 2.0, the instance at which softening, followed by failure, would occur.

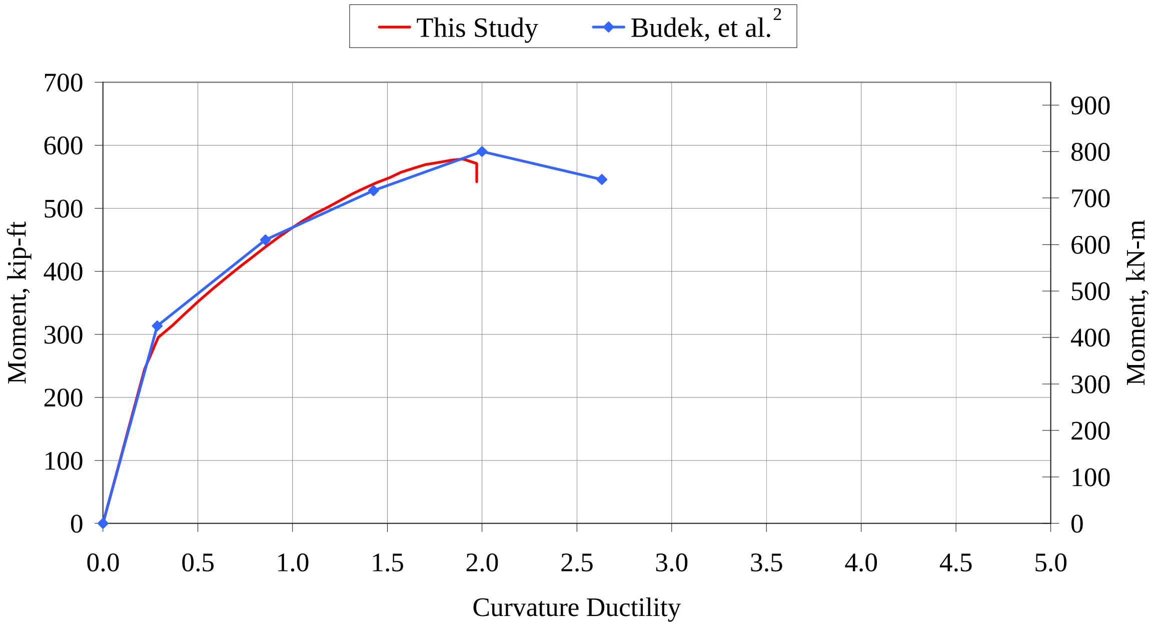

Fig. 8: Comparison of XTRACT and Test Results for PS13

ABAQUS ANALYSES

Load is plotted against displacement ductility for both PS12 and PS13 specimens in Figures 9 and 10, respectively. Displacement ductility is defined as the displacement at any time, *t*, to displacement at yield. It should be noted that displacement ductility of one for PS12 and PS13 were specified in the experimental work as 13 mm (0.5 in.) and 20 mm (0.79 in.), respectively. The performance of both specimens was governed by the tensile capacity of the unconfined concrete. Tensile cracks propagated into the cross section, which was indicated by the incremental reduction in stiffness in the initial post-yielding region of the curves. Once tensile cracks extended through the tension side of the pile up to the neutral axis which had, in the process, shifted upward, a nearly linear response followed until compressive failure began at the opposite pile surface. At that point, convergence was unattainable and the analysis was terminated. Incipient formation of tensile cracks occurred immediately after yielding in both models at an end reaction of approximately 150 kN (33.7 kip). These results agreed well with those from testing. From the slope of the curves, it is apparent that the post-cracking stiffness of the model and the ductility at failure also match those of the experiments. The difference in the experimental and analytical curves is that damage initiated earlier in the test specimens. Figures 9 and 10 illustrate that both FE models are able to accurately predict the initial and post-yield stiffness of the experimental results. Both models, however, over-predict the yield load by approximately 14 percent. In addition, both models over-predict the peak load by 8 percent for specimen PS12 and 20 percent for specimen PS13. These over-predictions could again be attributed to the fact that the analytical model was loaded monotonically rather than cyclically.

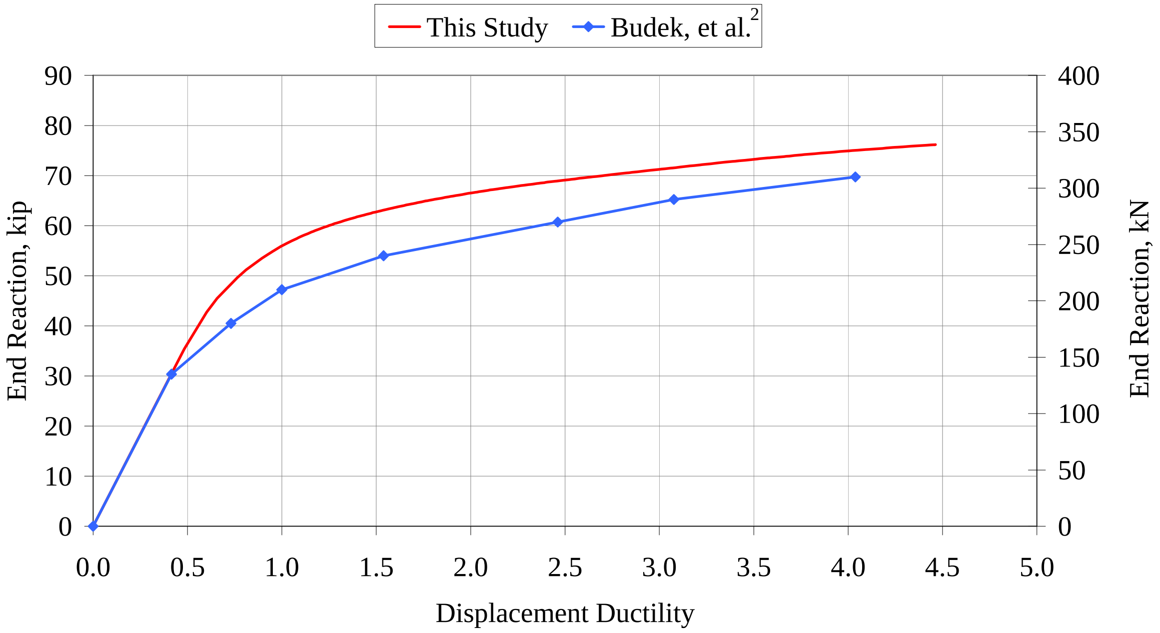

Fig. 9: Comparison of Finite Element and Test Results for PS12

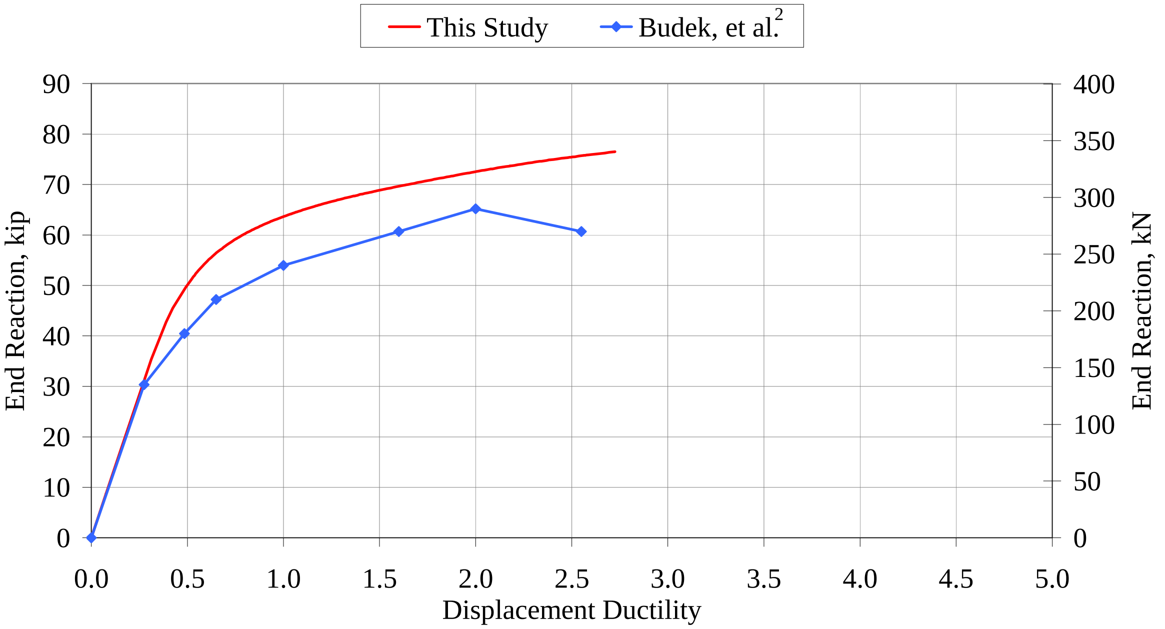

Fig. 10: Comparison of Finite Element and Test Results for PS13

Failure in both 3D finite element models was quantified by monitoring the compression damage variable in the output database. To facilitate this discussion, PS12 will be the model in reference. As previously mentioned in the discussion of the concrete constitutive model, spalling of concrete occurred at a compressive strain of 0.0027, which corresponds to 19 percent compression damage. In addition, once concrete spalled to the depth of the tendons and hoop reinforcement, failure was noted for the experimental specimens. By setting an upper limit for the contour plot of compression damage to 19 percent and looking at the last increment of the monotonic push phase, the distribution of compression damage in the pile cross section could be seen as shown in Figure 11. By inspection of Figure 11, one can see that the compressive damage during the last increment of the analysis is over 16 percent. The analysis of the model was not able to progress any further due to material convergence issues. This indicated that the current condition of the model is unstable and spalling of the concrete to the depth of the prestressing tendons and hoop reinforcement is imminent.

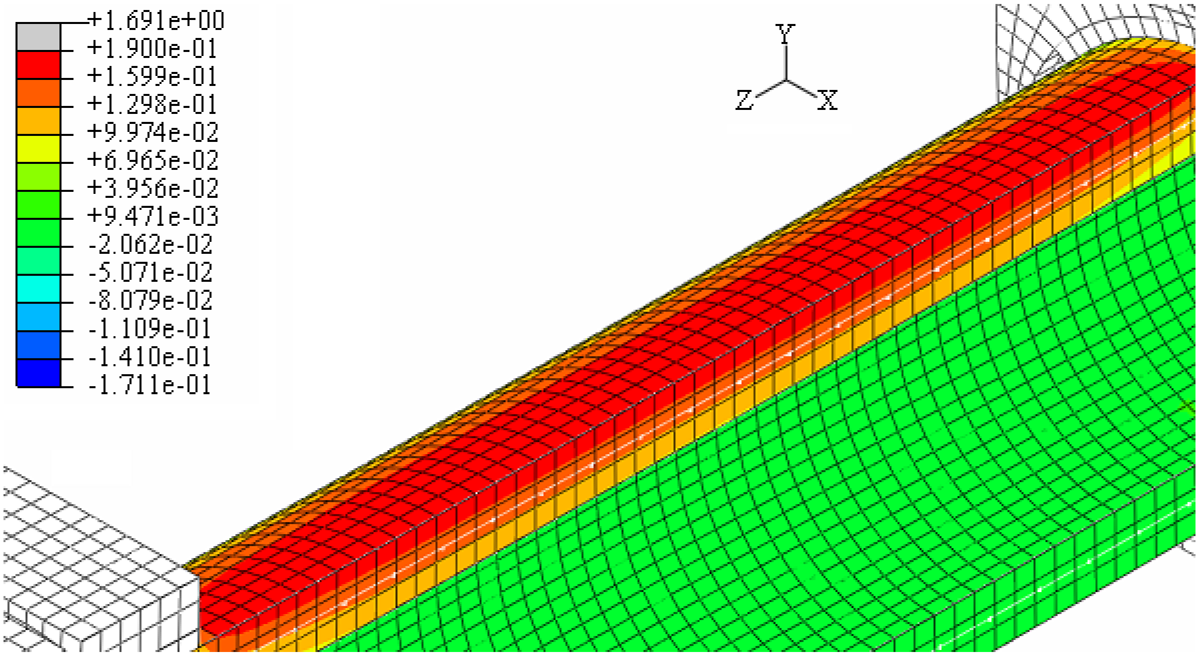

Fig. 11: Contour Plot of Compression Damage in PS12

To supplement the analytical evidence that failure in the FE models agrees with mechanisms observed by Budek, et. al[2], vector plots of plastic strain were also generated. A typical vector plot of this nature is given in Figure 12. When looking at the plot of plastic strain for the final increment of the analysis, it is important to note that on the outer surface the maximum principal plastic strain, minimum principal plastic strain, and mid principal plastic strain occurs in the *y*-, *z*- and *x*-axis directions, respectively. This indicated that the concrete on the exterior surface was being thrust away from the reinforcing steel and prestressing strands due to large compressive stress in the longitudinal direction. Upon examination of the inner surface of the pile, the maximum principal plastic strain occurs in the *x*-direction, while the minimum and mid principal plastic strains occur in the *z*- and *y*- directions, respectively. This three dimensional behavior and the resulting effect on damage is not included in the cross sectional analysis of XTRACT and it suggests that the concrete inside the confines of the hoop reinforcement responds similarly to confined concrete, but not appreciably so in terms of stress capacity.

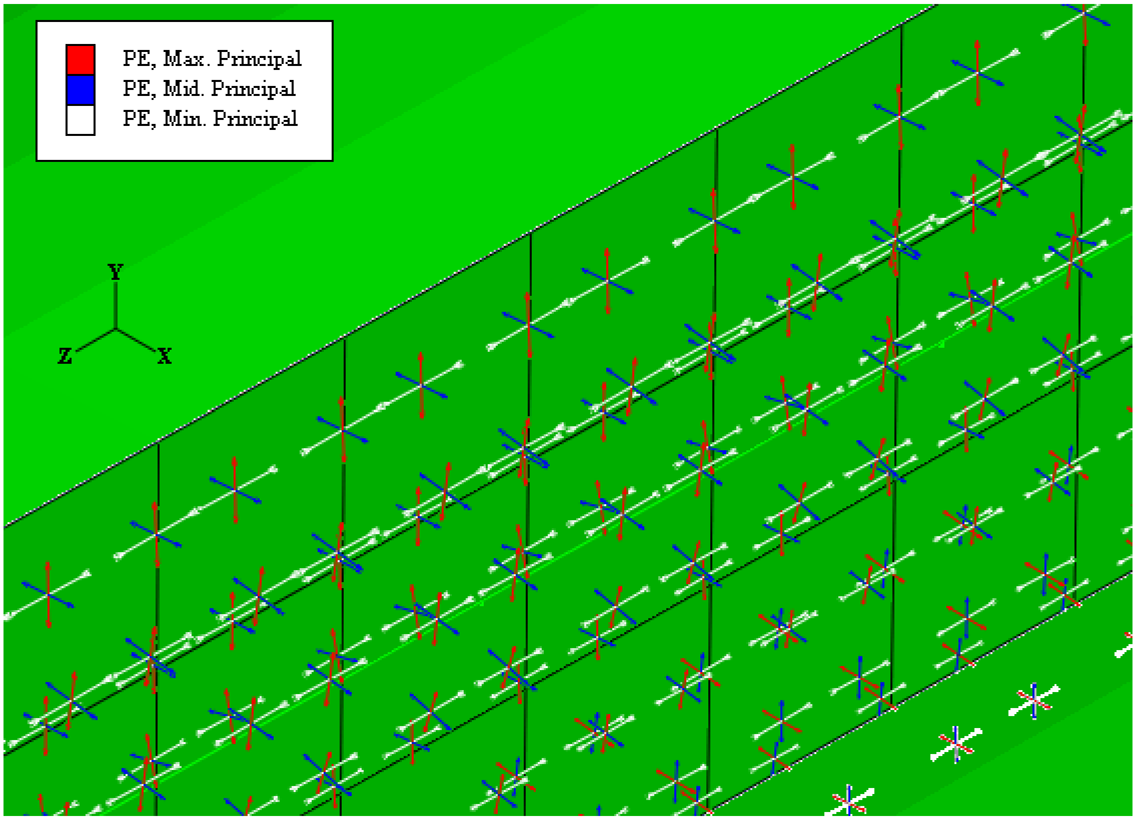

Fig. 12: Principal Plastic Strain Distribution

SAP2000 ANALYSES

A comparison of results from ABAQUS and SAP2000 for specimens PS12 and PS13 are provided in Figures 13 and 14, respectively. From Figures 13 and 14, it is evident that SAP2000 under-predicts displacement ductility by an average of 35 percent for both piles. However, it predicted quite well the strength of both piles. The under-predictions of displacement from SAP2000 is due to two factors: 1) under-predictions of the ultimate curvature of the pile cross section as shown in the XTRACT results, and 2) plastic hinge length determination. As shown in the figures, doubling the plastic hinge length nearly doubles the maximum displacement ductility for both piles. Moreover, this observation clearly illustrates the fact that careful consideration must be taken when calculating plastic hinge length since it drastically affects model performance.

Overall, the simplified method of using XTRACT in combination with SAP2000 provides a reasonable and conservative estimate of pile performance when plastic hinge length is calculated per Caltrans recommendations.

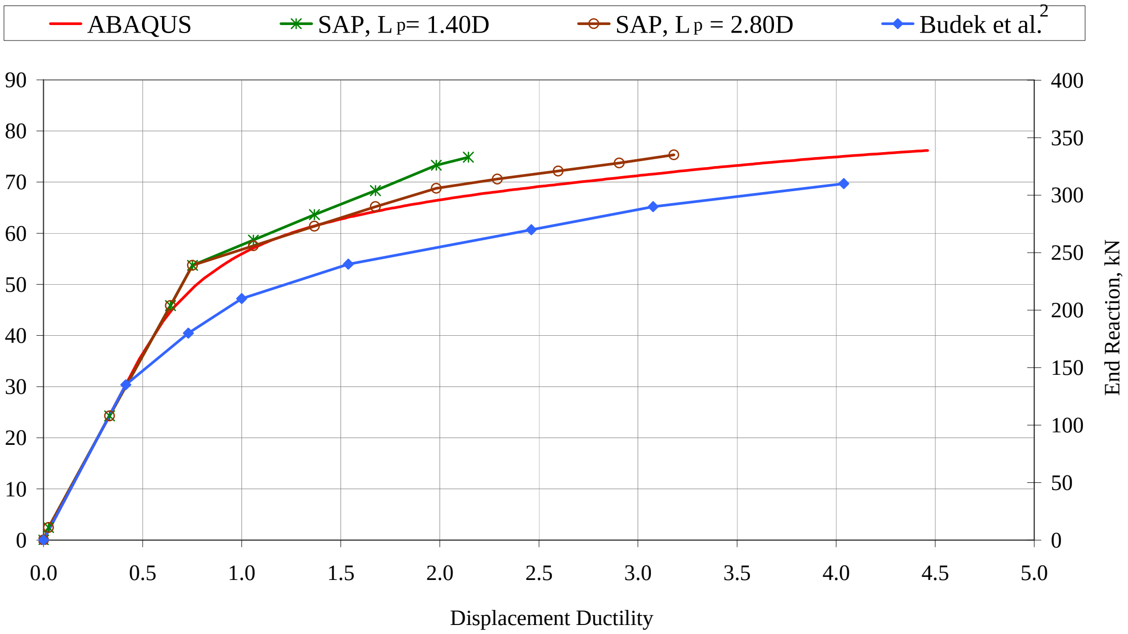

Fig. 13: Comparison of Results for Specimen PS12

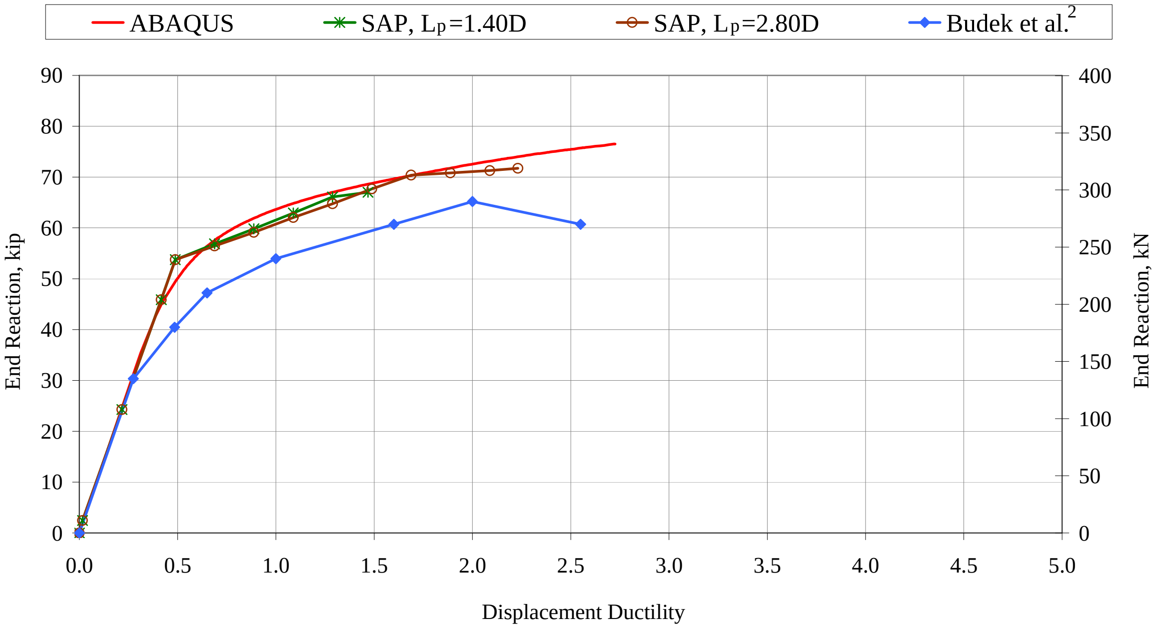

Fig. 14: Comparison of Results for Specimen PS13

CONCLUSIONS

Results from both the simplified (XTRACT/SAP2000) and detailed (ABAQUS) finite element models are summarized as follows:

- Failure occurs once concrete in the compression zone spalls, exposing the reinforcing steel and prestressing tendons.
- Load capacity and displacement ductilities at yield and failure appear to be well-predicted by ABAQUS.
- Cross sectional analysis appears to be adequate for predicting moment capacity. However, it does not reflect the damage and loss of stiffness from cyclic loading of the concrete without longitudinal reinforcement.
- ABAQUS is able to accurately predict the response of both PS12 & PS13 pile configurations.
- ABAQUS provides more accurate results for ductility than XTRACT. This could be attributed to the fact that ABAQUS includes the effect of triaxial stress from hoop reinforcement in the concrete failure response, while XTRACT only considers uniaxial behavior.
- Careful consideration must be taken when specifying the plastic hinge length for SAP2000 analyses since it can lead to drastic over or under-prediction in displacement ductility.
- XTRACT cross section analyses combined with SAP2000 pushover analyses provide reasonable and conservative approximations for pile performance when the plastic hinge length is defined per Caltrans Seismic Design Criteria.[18] For this work, displacement ductility capacity was under-estimated by an average of 35 percent when using this simplified approach.

ACKNOWLEDGEMENTS

This research was performed at Washington State University in the Department of Civil and Environmental Engineering. Funding for this research was provided by the Washington State Department of Transportation (WSDOT) under Project No. 5200. Their assistance is greatly appreciated.

REFERENCES

1. Budek, A.M., Benzoni, G., Priestley, M.J.N., “Analytical Studies on the Inelastic Seismic Response of Solid and Hollow Precast Prestressed Piles,” *Caltrans Report Number SSRP97/16*. November 1997.
2. Budek, A.M., Benzoni, G., Priestley, M.J.N., “Experimental Investigation of Ductility of In-Ground Hinges in Solid and Hollow Prestressed Piles,” *Caltrans Report Number SSRP97/17*. November 1997.
3. ABAQUS Software and Documentation, Version 6.7-1. © Dassault Systèmes, 2007.

4. XTRACT Software and Documentation, Version 3.0.8. TRC/Imbsen Software Systems Inc, 2001.
5. SAP2000 Advanced Nonlinear Software and Documentation, Version 11.0.4. Computers & Structures, Inc, 2007.
6. Collins, M.P., Mitchell, D., *Prestressed Concrete Structures*. Englewood Cliffs, NJ: Prentice Hall, ©1991, pp. 81-87.
7. American Concrete Institute Committee 318, *Building Code Requirements for Structural Concrete (ACI318-05) and Commentary (ACI318R-05)*. American Concrete Institute, Farmington Hills, MI. August 2005.
8. Iravani, S., "Mechanical Properties of High-Performance Concrete," *ACI Materials Journal,* V. 93, No. 5, September-October 1996, pp. 416-426.
9. Bae, S., Bayrak, O., "Stress Block Parameters for High-Strength Concrete Members," *ACI Structural Journal,* V. 100, No. 5, September-October 2003, pp. 626-636.
10. Hillerborg, A., Modeer M., Petersson P. E., "Analysis of Crack Formation and Crack Growth in Concrete by Means of Fracture Mechanics and Finite Elements," *Cement and Concrete Research*, V. 6, pp. 773–782, 1976.
11. Roesler, J., Paulino, G.H., Park, K., Gaedicke, C., "Concrete Fracture Prediction Using Bilinear Softening", *Cement and Concrete Composites*, V. 29, No. 4, April 2007, pp. 300-312.
12. Boresi, A.P., Schmidt, R.J., Sidebottom, O.M., Table 15.2, Case 4. Single-Edge Crack in Finite-Width Sheet, *Advanced Mechanics of Materials*, 5th Edition, © John Wiley & Sons, 1993, pp. 614-615.
13. Darwin, D., Barham, S., Kozul, R., Luan, S., "Fracture Energy of High-Strength Concrete," *ACI Materials Journal*, V. 98, No. 5, September-October 2001, pp. 410-417.
14. Appa Rao, G., Raghu Prasad, B.K., "Fracture Energy and Softening Behavior of High-Strength Concrete," *Cement and Concrete Research*, V. 32, No. 2, February 2002, pp. 247-252.
15. Einsfeld, R.A., Velasco, M.S.L., "Fracture Parameters for High-Performance Concrete," *Cement and Concrete Research* V. 36, No. 3, March 2006, pp. 576-583.
16. MatWeb, "Advanced Elastomer Systems Geolast® 701-70 Thermoplastic Rubber," http://www.matweb.com/search/datasheet.aspx?matid=22596, accessed January 16, 2008.
17. Greenwood, S.M., *Analytical Performance Evaluation of Hollow Prestressed Piles and Pile-Cap Connections in the I5 Ravenna Bridge*, M.S. thesis, Washington State University, 2008 (In-Preparation).
18. *Caltrans Seismic Design Criteria (CSDC) Version 1.4*, California Department of Transportation, Section 7, June 2006.